PHYSICS OF PLASMAS **17**, 055501 (2010)

Applied spectroscopy in pulsed power plasmas[a)]

G. A. Rochau,[1,b)] J. E. Bailey,[1] and Y. Maron[2]
[1]*Sandia National Laboratories, Albuquerque, New Mexico 87185-1196, USA*
[2]*Faculty of Physics, Weizmann Institute of Science, Rehovot 76100, Israel*

(Received 20 November 2009; accepted 14 December 2009; published online 11 March 2010)

Applied spectroscopy is a powerful diagnostic tool for high energy density plasmas produced with modern pulsed power facilities. These facilities create unique plasma environments with a broad range of electron densities ($10^{13}-10^{23}$ cm^{-3}) and temperatures ($10^{0}-10^{3}$ eV) immersed in strong magnetic (>100 T) and electric (up to 1 GV/m) fields. This paper surveys the application of plasma spectroscopy to diagnose a variety of plasma conditions generated by pulsed power sources including: magnetic field penetration into plasma, measuring the time-dependent spatial distribution of 1 GV/m electric fields, opacity measurements approaching stellar interior conditions, characteristics of a radiating shock propagating at 330 km/s, and determination of plasma conditions in imploded capsule cores at 150 Mbar pressures. These applications provide insight into fundamental properties of nature in addition to their importance for addressing challenging pulsed power science problems. © *2010 American Institute of Physics*. [doi:10.1063/1.3309722]

I. INTRODUCTION

The conditions and environment of a plasma affect the ionization state of the constituent elements, the bound atomic energy states, and the distribution of electrons among the bound states. Observing electron transitions between the bound energy states (recording either emission or absorption spectra) provides a measure of the ionization and bound energy state distributions that can be used to infer the plasma conditions. The information encoded in the measured spectra can include the plasma composition, electron temperature, ion temperature, electron density, ion velocity, and electric and magnetic field strengths. Thus, detailed spectroscopic data can, in principle, provide a wealth of information. Decoding this information requires line intensity, line shape, and line position analysis through the comparison of the recorded spectra with synthetic spectra computed from the modern theories of atoms in plasmas. Accurate determination of plasma conditions from recorded spectra therefore depends on the accuracy of atomic theory, the theory of atoms in plasma, and the coupling of these theories with radiation transport.

Spectroscopic diagnostics have been applied to understand a very broad range of plasmas both in the laboratory and throughout the universe. Figure 1 shows a phase-space plot of plasma temperature versus density showing the nominal conditions of a variety of laboratory and space plasmas that are diagnosed using spectroscopic techniques. The figure delineates the high energy density (HED) regime of plasma physics, which is defined as plasmas with a total energy density of $>10^{11}$ J/m^{3} (corresponding to a pressure of 1 Mbar).[1] Also shown in Fig. 1 is the broad range of plasma temperature and densities that can be achieved in the laboratory using pulsed power sources.

Pulsed power is a general term that describes the compression of electrical energy in space and time to provide high electrical power to various types of electrical loads, such as microwave cavities, ion beams, and z pinches.[2,3] The production of hot dense matter requires a technology called high pulsed power, which has an energy store of up to a few tens of megajoules and can produce electrical powers up to 10^{15} W. To set this in perspective, modern pulsed power machines can time compress the equivalent electrical energy consumption in one evening's operation of a TV set (a few megajoules) into more electrical power than provided by all the power plants in the world combined (~ 15 TW).[2] Before the advent of lasers, pulsed power sources were the preferred method of producing plasmas in the laboratory and played a critical role in producing the experimental data that was used to benchmark the modern theory of spectral line shapes.[4,5] Since the 1980s, spectroscopy has been applied to understand the detailed operation of a variety of pulsed power sources including applied-B ion diodes, plasma opening switches, and z pinches. In the application of spectroscopy to understand a particular aspect of these pulsed power technologies, spectroscopy by its very nature elucidates various aspects of the fundamental physics involved. This paper describes examples of these fundamental measurements across three main categories: the determination of magnetic field penetration in plasma, the determination of electric fields in non-neutral plasma, and the determination of plasma conditions in HED plasmas.

II. MAGNETIC FIELD MEASUREMENTS

The penetration of magnetic fields (B-fields) in plasma is an issue of general importance that matters for a variety of space plasmas (i.e., solar flares, the interaction of the solar wind with Earth's magnetosphere) as well as for a variety of pulsed power systems. The evolution of a B-field in plasma is given by the expression

---

[a)] Paper WR1 1, Bull. Am. Phys. Soc. **54**, 342 (2009).
[b)] Invited speaker.

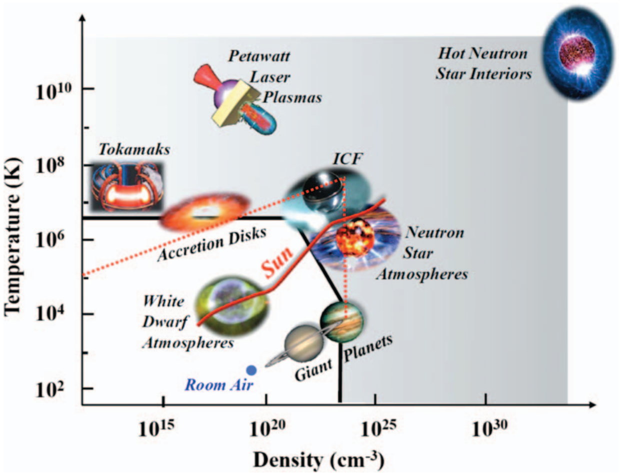

FIG. 1. (Color) Phase-space plot of temperature vs number density including approximate conditions of interest for a variety of laboratory and space plasmas. The shaded area indicates the HED regime where an equilibrium plasma contains a total energy density of $>10^{11}$ J/m^3. The red-dashed line indicates the approximate upper bound for demonstrated conditions of pulsed power produced plasmas.

$$\frac{dB}{dt} = \frac{\eta}{\mu_0}\nabla^2 B - \nabla \times \left(\frac{J \times B}{en_e}\right) + \nabla \times (v_i \times B), \qquad (1)$$

where B is the magnetic field vector, J is the current, v_i is the ion velocity, n_e is the electron density, e is the electron charge, η is the plasma resistivity, and μ_0 is the permeability of free space. The right hand side of Eq. (1) has three terms: The first is the diffusion term, the second is the Hall term, and the third is the convection term. Any of these terms can dominate the B-field evolution depending on the conditions of the plasma and can be influenced by both spatial variations in the plasma properties and instabilities. Understanding the process that dominates in a particular plasma requires determining the speed of the B-field penetration and/or the B-field distribution.

Zeeman splitting is the most commonly used spectroscopic method for B-field measurements. In Zeeman splitting, an external B-field interacts with the total orbital angular momentum of the various energy states in the atom through the magnetic moment, which is quantum mechanically described by the quantum number M. Under the influence of the B-field, the bound energy states shift by an amount proportional to the product of the quantum number M with the magnetic field strength. When electrons transition from these split energy levels, one observes a splitting of the spectral line proportional to the strength of the B-field. One important aspect of these Zeeman split components is that they come in two different polarizations. Those transitions with no change in M between the upper and lower levels are linearly polarized (the π components) resulting from electric dipole oscillations along the B-field direction. Those transitions with a change in M of ±1 are circularly polarized (the σ components) resulting from oscillations perpendicular to the B-field direction. Observations made along the B-field direction will therefore only include the σ components, which are more affected by the magnetic field.

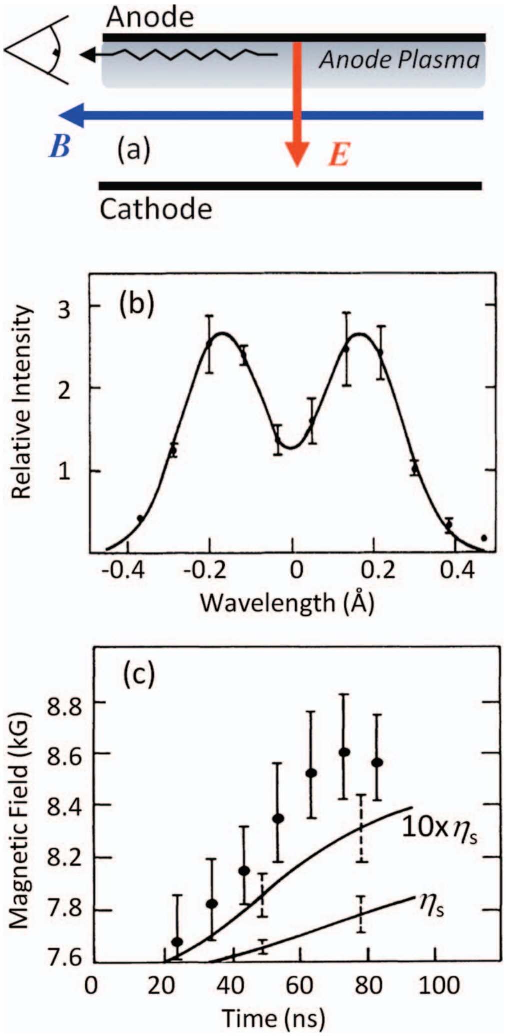

FIG. 2. (Color) (a) Schematic representation of an applied-B ion diode. (b) Example measured (points) and calculated (line) Zeeman split line profile measurement of the Ba II 5d-6p transition centered at 6142 Å from the anode plasma indicating a B-field of ~7.5 kG. (c) Time-dependent measured (points) and calculated (lines) B-field in the anode plasma. The calculations assume a diffusive penetration at the classical Spitzer resistivity, η_S, and at an anomalous resistivity ten times higher than the Spitzer value. Adapted from Ref. 6.

Maron *et al.*[6] used spectral measurements of Zeeman splitting to study the B-field dynamics in an applied-B ion diode [Fig. 2(a)]. This is an anode-cathode gap with an applied pulsed voltage that accelerates ions from the anode, creating an ion beam. The applied voltage also accelerates electrons from the cathode, requiring the application of a B-field to trap the electrons and prevent them from crossing the gap and shorting out the diode. Maron and colleagues measured the time-dependent line profile of the 5d-6p transition of singly ionized barium centered at 6142 Å [Fig. 2(b)]. Barium was introduced as a dopant on the anode side of the diode where the Ba II ionization state remains localized in the anode plasma a few microns from the original anode surface. This anode plasma was measured on separate experiments to have an electron density of 2×10^{15} cm^{-3} and an electron temperature of 7 eV.[7] Under these plasma conditions the observed line shape is dominated by the Zeeman splitting. Several mechanisms can influence spectral line profiles so determining their relative impact is an important consideration when using line shapes for plasma diagnostics. The measurements are made along the direction of the applied magnetic field so that only the σ line components are observed, resulting in a measured line profile that is symmetrically split by a relative amount that depends on the B-field strength. Figure 2(c) shows the time-dependent B-field within a few microns of the original anode surface. The field is observed to increase over the applied 7.6 kG. This increase is caused by E×B drifting electrons, which create a diamagnetic field that decreases the field strength near the cathode, requiring an increase in the field on the anode side in order to conserve magnetic flux. Magnetic diffusion is expected to dominate the field penetration for this geometry at these conditions, but a classical Spitzer resistivity predicts a much slower diffusion speed than was measured. Maron *et al.* must assume an anomalous resistivity greater than ten times the Spitzer value in order to explain the data. This anomalous resistivity was later explained as being caused by instabilities in the anode plasma that increase the collision frequency and therefore, also the resistivity.[8,9] These measurements are an example of how real world effects, such as instabilities, can significantly alter the field penetration over a simple idealized picture.

A second important measurement of B-field penetration in plasma was made by Arad *et al.*[10] using a plasma opening switch [Fig. 3(a)]. In this system, a pulsed voltage is applied between an anode-cathode gap that is intentionally filled with CH plasma having an initial electron density of $(3-7) \times 10^{14}$ cm^{-3} and a temperature of 6.5 eV.[11] This plasma shorts out the diode until the magnetic field can penetrate all the way through, which can be an effective way to sharpen the current rise downstream of the plasma. Arad *et al.* measured the time and space-dependent B-field in the CH plasma by injecting a localized plume of He and observing the neutral He 2p-3d transition [Fig. 3(b)]. Again, the transition was measured in emission from a direction parallel to the B-field so that they only measured the circularly polarized components. The time- and space-dependent B-field was measured by observing the time-dependent Zeeman splitting of the He 2p-3d transition in the localized area of the He plume and then moving the plume location through the plasma along the z direction on subsequent experiments. Figure 3(c) shows the changing B-field distribution as the field penetrates the plasma. Not only does the B-field penetrate faster than would be expected for diffusion, but the shape of the penetration front is different from that predicted by diffusion theory so the penetration speed cannot be attributed simply to anomalous resistivity. In the geometry of this plasma opening switch, it can be shown that the Hall term to the field evolution can become dominant if large density gradients exist in the plasma along a direction opposing the current flow. The natural gradient of the plasma from the injection into the gap is not large enough to explain the penetration, but Arad *et al.* suggested that instabilities in the plasma create gradients along a small-enough spatial scale to make this term dominant, and produces a penetration speed and shape that is consistent with the data. Later measurements of the field penetration front[12] further support a theory of Hall penetration.[13,14] While the possibility of fast magnetic field penetration into low resistivity plasmas was raised due to B-dot loop measurements,[15] it was the spectroscopic diagnostics that demonstrated the penetration reliably and yielded the evolution of the B-field distribution in the plasma.[10–12,16,17]

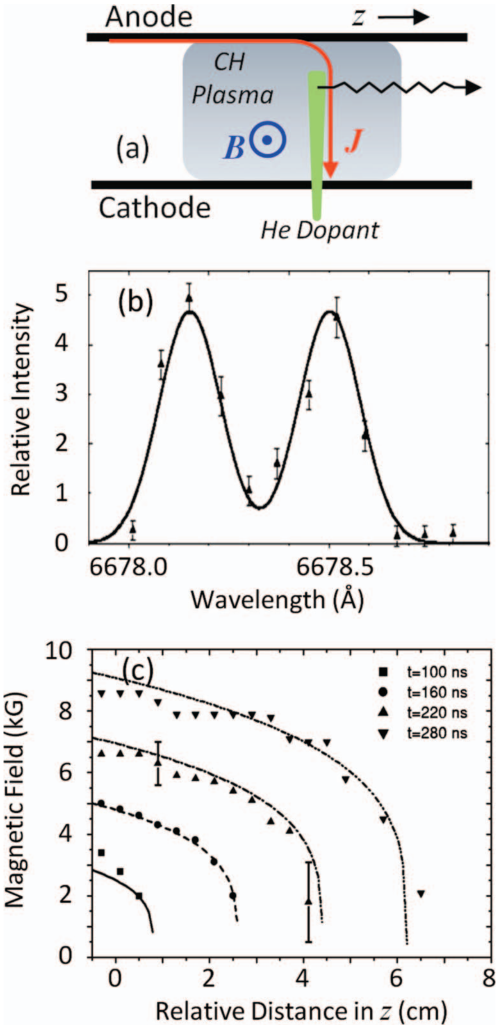

FIG. 3. (Color) (a) Schematic representation of a plasma opening switch, in which a He dopant is introduced to measure the local B-field. Emission from the He dopant is measured parallel to the B-field from a direction normal to the page. (b) Example Zeeman split line profile measurement of the He I 2p-3d transition indicating a B-field of ~9.2 kG. (c) Measured B-field distribution at various times during the operation of the opening switch (points). The speed and distribution of the B-field contradicts penetration by magnetic diffusion. Adapted from Ref. 10.

A third important example of B-field penetration into a plasma was made by Davara *et al.*,[18] who were studying the dynamics of a CO$_2$ gas-puff z pinch [Fig. 4(a)]. A z pinch is a cylindrical column of plasma through which a pulsed current that creates an azimuthally directed B-field is applied. The resulting $J \times$B force is directed radially inward and converts the electrical energy into kinetic energy. The z-pinch plasma stagnates on axis creating a shock that converts the kinetic energy into thermal energy, which is radiated away as x rays. Knowledge of the B-field distribution in plasmas imploding under magnetic fields is a crucial factor in under-

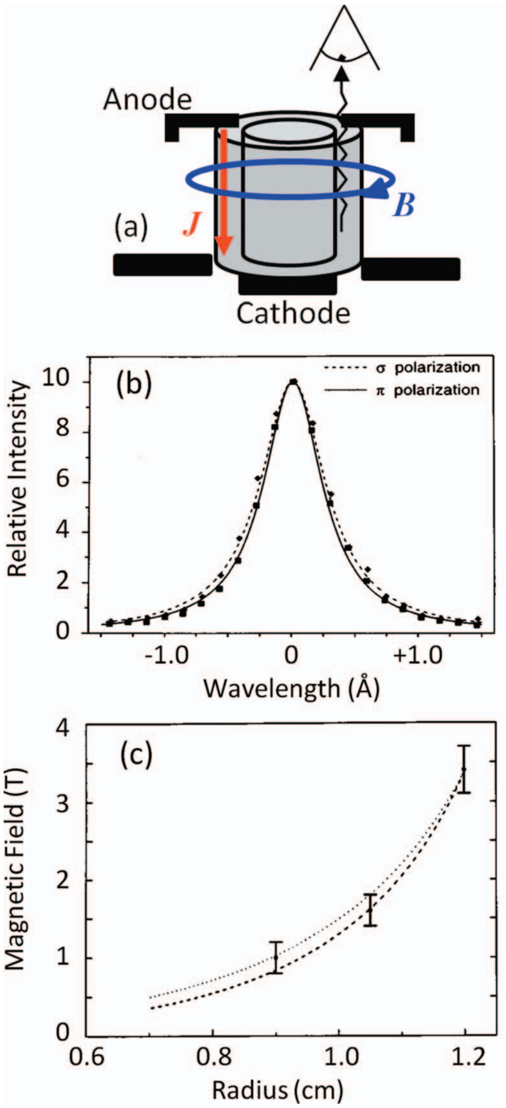

FIG. 4. (Color) (a) Schematic representation of a gas-puff z pinch. (b) Example line profile measurement (points) and calculation (lines) of the linearly (square points, solid line) and circularly (diamond points, dashed line) polarized components of the O IV 3s-3p line emission from oxygen in the gas puff indicating a B-field of ~1.8 T. (c) Measured B-field distribution in the z-pinch plasma at one time during the implosion (points). Calculations assuming diffusive B-field penetration at a resistivity of 45 $\mu\Omega$ m (dotted line) and 32 $\mu\Omega$ m (dashed line) are in close agreement to the classical Spitzer value of ~48 $\mu\Omega$ m. Adapted from Ref. 18.

standing the implosion dynamics. Davara *et al.* measured the B-field distribution in the z pinch using time- and space-resolved measurements of the Zeeman splitting of the O IV 3s-3p line emission [Fig. 4(b)]. In this case, the CO_2 plasma electron density and temperature over the duration of the measurements are $\sim 5\times 10^{17}$ cm^{-3} and 5–13 eV, respectively.[19,20] Stark broadening[4,5] dominates the line profile under these conditions, which smears out the measurable effect of the Zeeman splitting. To determine the magnetic field strength, Davara *et al.* separately measured the linear and circularly polarized line components by observing the O IV 3s-3p emission perpendicular to the B-field direction and using a quarter-wave plate to separate the different polarizations. The circularly polarized components are always more affected by Zeeman than the linear components, but the Stark and Doppler effects are similar for both allowing one to separate out the B-field effect by measuring the difference in the width of the polarized components [Fig. 4(b)]. The measurements were made by averaging over ~20 experiments in order to obtain a signal-to-noise ratio sufficient to conclusively measure the small difference in the widths of the polarized components. Figure 4(c) shows the radially dependent B-field in the CO_2 gas-puff z pinch at a time corresponding to about half-way through the z-pinch implosion. In this case, the B-field has a profile that is consistent with magnetic diffusion at the rate predicted by the classical Spitzer resistivity. The density of the plasma is high enough that electron collisions dominate the plasma resistivity and the diffusion term dominates the B-field penetration. In addition to the general interest of the B-field penetration, these data are also critical to solving the energy balance in a z-pinch plasma. Combining these data with other spectroscopic measurements of the electron temperature, density, and ion velocity, Gregorian *et al.*[19–21] were able to demonstrate that ~85% of the energy imparted to their z pinch comes from the $J\times$B force with the remainder coming from the Joule heating.

Extending these examples of the Zeeman split B-field measurements to HED plasmas has many challenges. As the temperature and density of the plasma increase, separating out the Zeeman effect from the other competing line broadening components becomes more difficult. In addition, HED plasmas can be turbulent containing fields of various directions in the plasma region viewed, they may have rapid spatial or temporal gradients, and the high cost of creating HED plasmas requires that diagnostic information be obtained in a single shot. One potential approach to solving these issues was recently proposed by Stambulchik *et al.*[22] They showed that the transitions from certain fine-structure components can have similar Stark and Doppler broadenings, but always have different Zeeman splitting regardless of either the field strength or which polarization components are observed. This makes it possible to measure nondirectional B-fields in plasmas that may also have spatial and/or temporal gradients. In addition, the fine-structure components also lie close in wavelength making it possible to observe each line profile on a single spectrometer allowing for higher measurement accuracy. Stambulchik *et al.* demonstrated this technique with measurements of the $^2P_{1/2}$ and $^2P_{3/2}$ components of the Al III 4p-4s transition in a plasma with an electron density and temperature of 2×10^{16} cm^{-3} and 10 eV, respectively [Fig. 5]. The $^2P_{1/2}$ component is always more affected by the Zeeman splitting allowing one to determine the magnetic field strength from the difference in the line shapes between the two fine-structure components. This technique is highly promising in being extended to HED plasmas by selecting the transitions appropriate for the plasma properties and field strengths of interest.

III. ELECTRIC FIELD MEASUREMENTS

Another important category of spectroscopic measurements is the determination of electric fields (E-fields). In a non-neutral plasma, combining measurements of the E-field

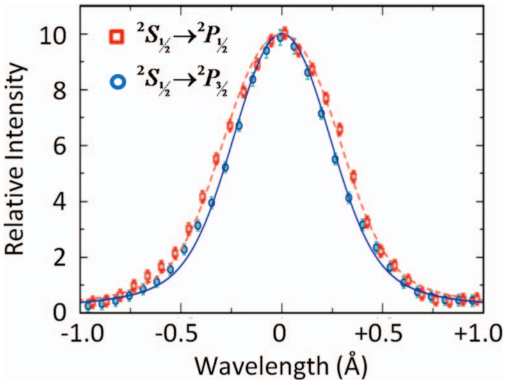

FIG. 5. (Color) Line profile measurements (points) and calculations (lines) of the fine-structure components from the Al III 4s-4p doublet transition indicating a B-field of 0.9 T. Adapted from Ref. 22.

with a determination of the ion current provides a wealth of information. Energy conservation yields the ion velocity through the relation

$$v_i^2 = 2\frac{Ze}{m_i}\int \mathrm{E}dx, \tag{2}$$

where Z is the ion charge state and m_i is the ion mass. Beam current measurements yield the ion density distribution through the relation

$$n_i = \frac{J_i}{Zev_i}, \tag{3}$$

where J_i is the beam current. Finally, Gauss' law yields the electron density distribution, $\mathrm{n_e}$, through the relation

$$\nabla \cdot \mathrm{E} = 4\pi \mathrm{e}(Z\mathrm{n}_i - \mathrm{n_e}). \tag{4}$$

The Stark effect is the electric field analog to the Zeeman effect and provides a spectroscopic signature for E-field measurements. In this case an external E-field induces an electric dipole moment in the atoms proportional to the field strength, which gives rise to an energy of interaction proportional to E^2. In the quadratic Stark effect, the energy level shift depends on the product of E^2 with the polarizability of the level, which depends on the square of the quantum number M. The degeneracy of the levels is therefore only partially lifted and those levels with the same absolute value of M shift by the same amount in the same direction. What is observed is therefore a partial splitting and shifting of the characteristic line radiation that can be used to determine the E-field strength.

Maron *et al.* made the first Stark shift E-field measurements in an ion diode gap[23,24] [Fig. 2(a)]. In these experiments, a thin aluminum coating was added to the anode, which formed doubly ionized aluminum that is accelerated across the gap. To measure the time-dependent E-field distribution, the Stark shift of the Al III 4d-4p transition at 4529 Å was observed using a spectrograph with both temporal and spatial resolution. This line is used because the upper state has a lifetime on the order of the transit time across the gap, and the emission comes from high-lying levels where the Stark effect is maximized. An example of the measured line profile at a particular place and time in the diode gap is shown in Fig. 6(a) where the unshifted component is determined to be scattered light originating from the anode plasma and the shifted component at longer wavelength corresponds to an electric field of 1.2–1.5 MV/cm. Figure 6(b) shows the measured E-field distribution in the diode gap at one time, which peaks at ~0.8 MV/cm near the anode and decreases to ~0.4 MV/cm near the cathode. Using Eqs. (2)–(4), Maron *et al.* made the first electron density profile determination in an ion diode gap and showed the occurrence of electrons close to the anode. This was in contradiction to contemporary Brillouin-flow models that predicted the electrons to stay near the cathode.[25] The migration of electrons across the gap had been experimentally inferred through measurements of ion currents, which were in excess of the Child–Langmuir limit. As theoretically showed by Desjarlais,[26] electrons near the anode will reduce the space charge causing a beam current enhancement and the eventual impedance collapse of the diode.

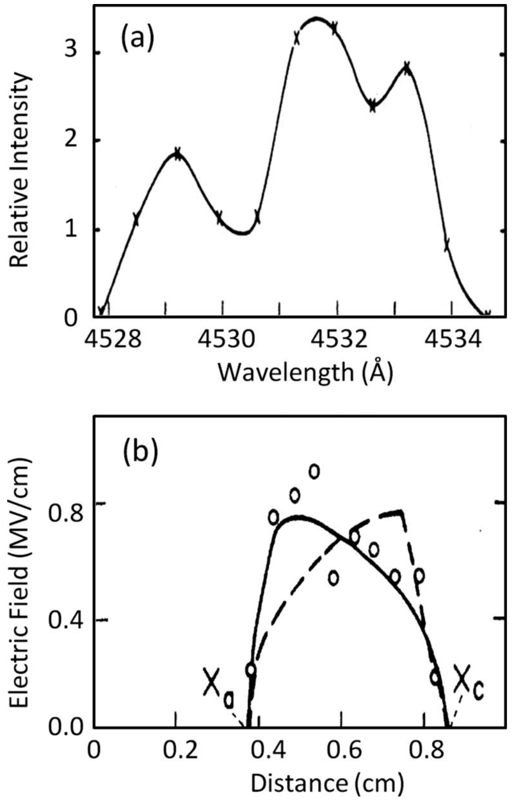

FIG. 6. (a) Example measurement of the Stark-shifted line profile of the Al III 4d-4p transition from an applied-B ion diode. (b) Measured (points) E-field distribution in the diode gap compared to a Brillouin-flow calculation of the distribution (dashed line). Adapted from Ref. 24.

Bailey *et al.* applied the Stark shift measurement technique to the Particle Beam Fusion Accelerator II (PBFA-II) ion diode at Sandia National Laboratories.[27] This was an ion diode with cylindrical symmetry intended to produce a Li ion beam for studies in inertial fusion.[28] To measure the E-field distribution in the diode gap, Bailey *et al.* measured the Stark shifting of neutral Li that gained energy as Li II from the anode, but charge exchange through a contaminant layer in the anode plasma and propagate across the gap at their origi-

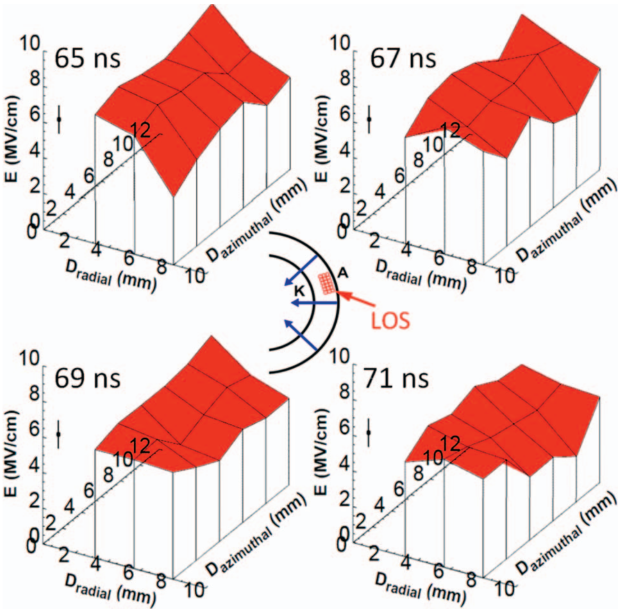

FIG. 7. (Color) Time- and multidimensional distribution of the E-field in the PBFA-II applied-B ion diode. The measurements are made using multiple streaked visible spectrometers to measure the time-dependent Stark shifting of the Li I 2s-2p transition from multiple LOSs covering a fraction of the radial and azimuthal extent of the diode gap.

nal kinetic energy. This charge-exchange process may be a contributing factor to the ion beam divergence, which has also been measured using spectral emission in both low[29] and high[30] power ion beam diodes. The E-field distribution in the PBFA-II ion diode was measured from the Stark shifting of the Li I 2s-2p transition and found to peak at 1 GV/m near the anode and decrease toward the cathode. Again using Eqs. (2)–(4), Bailey *et al.* determined the electron density distribution and determined that electrons fill the entire gap. The expansion of the electrons across the gap is likely related to instabilities, which can lead to fluctuations in the electric field. Measuring these fluctuations requires time- and multidimensional space-resolved spectra obtained on a single shot. Filuk and Bailey[31] measured the two-dimensional E-field distribution through an array of streaked optical spectrometers observing 18 separate lines of sight (LOSs) across a fraction of the radial and azimuthal extent of the diode gap. Again, the time-dependent E-field along each LOS was determined from the Stark shifting of the Li I 2s-2p transition and is shown in Fig. 7. This type of time-dependent, multidimensional measurement is critical to understanding the details of HED plasmas.

From a more basic science perspective, the Stark shift measurements on PBFA-II provided a unique opportunity to study the basic atomic physics of field ionization. As described above, the electric field was determined from the Li I 2s-2p transition. However, Bailey *et al.* also observed the Li I 2p-3d transition, which has a higher lying upper level that is more affected by the Stark effect.[32] The >5 MV/cm electric fields shift the 3d level completely into the continuum and the 2p-3d emission is not observed until the field falls below ~ 4 MV/cm (Fig. 8). When it is observed, the 2p-3d line is split into two components: One corresponding to the $|M|=0,1$ components of the 3d level and one corresponding to the $|M|=2$ component. These observations motivated the development and benchmarking of fundamental computations of the field ionization of various levels,[33] and led to the first models of polarizations induced by ion beam excitations.[34]

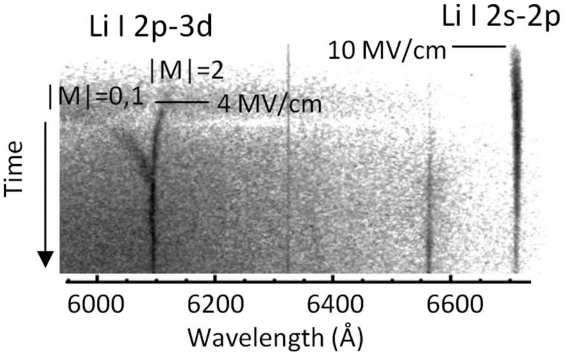

FIG. 8. Streaked spectra from the PBFA-II ion diode showing Stark-shifted time-dependent wavelength and line shape of the Li I 2s-2p and 2p-3d transitions. The 2p-3d transitions are not observed until the time-dependent E-field in the diode falls below ~ 4 MV/cm. When the 2p-3d transitions are observed, they are split into components corresponding to quantum numbers $|M|=0,1$ and $|M|=2$. Adapted from Ref. 32.

IV. HIGH ENERGY DENSITY PLASMA MEASUREMENTS

Breakthroughs in z-pinch technology first enabled the study of x-ray driven HED plasmas on pulsed power drivers in the 1990s when researchers began investigating the use of arrays of wires as the progenitor to the z-pinch plasma.[35–38] They studied the peak x-ray power output with the number of wires in the array and made a significant breakthrough. High number wire array z pinches were shown to be very effective x-ray power sources increasing the peak radiated power by orders of magnitude over what had been previously achieved.[36] Tungsten wire array z pinches on the Z facility at Sandia National Laboratories produce >1 MJ of x-ray energy at peak x-ray powers of >200 TW. The Z facility stores up to 25 MJ of electrical energy, produces peak electrical powers up to 100 TW, and is capable of delivering >24 MA of current to a z pinch. This technology is $\sim 10\%$ efficient in the conversion of stored electrical energy to x-ray emission energy. Experiments on the Z facility reach HED plasma conditions that address issues of fundamental importance including studies of Diamond at 10 Mbar pressure,[39] D_2 equation-of-state at >1 Mbar pressure,[40] photoionized plasmas,[41] radiating shocks,[42] the opacity of material at electron temperature >150 eV,[43] and studies in inertial confinement fusion (ICF).[44]

V. HED MEASUREMENTS: RADIATING SHOCKS

One of the most studied z-pinch platforms is the z-pinch dynamic *Hohlraum* (ZPDH).[42–51] The ZPDH delivers high-power x-ray pulses for a variety of HED physics applications including radiative transfer,[49] opacity measurements,[50] and ICF.[51] This system is composed of a 12 mm tall, 40/20 mm diameter outer/inner tungsten wire array, and a 6 mm diam-

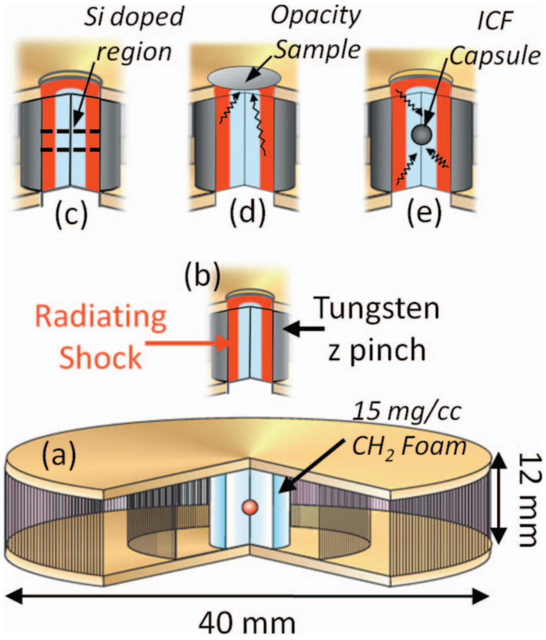

FIG. 9. (Color) (a) Schematic representation of the ZPDH, which is composed of a nested tungsten wire array and a 6 mm diameter CH_2 foam. (b) When the tungsten z pinch strikes the CH_2 foam, it launches a radiating shock. (c) The radiating shock conditions are diagnosed by doping the central 3 mm height of the CH_2 with 1% Si and spectrally resolving the Si emission from the shocked plasma. (d) The radiating shock is used to heat and backlight opacity samples at $T_e > 150$ eV placed across an aperture in the upper electrode of the ZPDH. (d) X-ray emission from the radiating shock and the re-emission from the tungsten z pinch drive ICF capsules to fusion conditions.

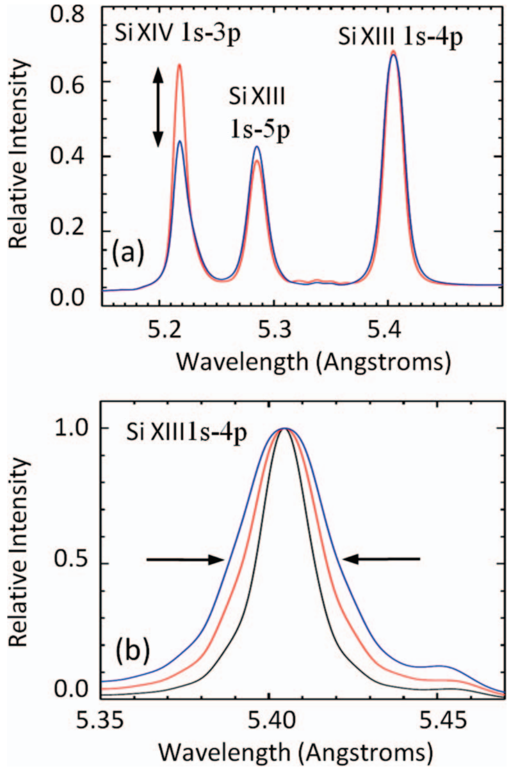

FIG. 10. (Color) (a) Calculated Si emission spectra from the radiating shock at $T_e = 330$ eV (blue) and 370 eV (red) showing the sensitivity of the spectra to changes in electron temperature. (b) Calculated line profile of the Si XIII 1s-4p transition at $\rho = 15$ mg/cm^3 (black), 25 mg/cm^3 (red), and 35 mg/cm^3 (blue) showing the sensitivity to changes in electron density.

eter 14.5 mg/cm^3 CH_2 foam converter [Fig. 9(a)]. The z pinch is imploded with a 100–130 ns long current pulse that peaks at 22–24 MA. During the implosion, the tungsten z pinch strikes the CH_2 converter launching a radiating shock [Fig. 9(b)]. This shock is driven ahead of the tungsten plasma leaving a layer of shocked CH_2. The shock propagates at 326 ± 25 km/s, has a driving pressure of 5–10 Mbars, and a shocked CH_2 temperature of 300–400 eV.

Rochau *et al.*[42] determined the conditions of the radiating shock in the ZPDH by observing self-emission of silicon that was doped into the central 3 mm height of the CH_2 foam [Fig. 9(c)]. The Si emission spectra are used to determine the shock conditions through comparison to collisional-radiative (CR) simulations. Under an assumed temperature and density distribution, CR simulations determine the ionization states, the bound state populations, and the associated x-ray emission by balancing the sum of all the populating rates with all the depopulating rates including both collisional and radiative excitation and ionization processes.[52,53] These calculations are done including accurate radiation transport in the geometry of the shocked plasma since the kinetics of any given plasma element can be effected by radiation from the entire volume. CR simulations show sensitivity of the observed Si spectra from the radiating shock to changes in electron temperature through the relative intensities of line and satellite emission from different ionization states [Fig. 10(a)]. They also showed sensitivity to changes in the density through the line shapes of 1s-np transitions, which are measurably affected by Stark broadening for $n > 2$ [Fig. 10(b)].

Determining the plasma conditions then requires a forward calculation search process with the following algorithm: (1) Assume a distribution of T_e and n_e. (2) Calculate the CR kinetics. (3) Calculate a synthetic spectrum as seen by the spectrometer. (3) Determine a goodness of fit between the synthetic and experimentally acquired spectra. (4) Repeat the process until the assumed plasma conditions produce a synthetic spectrum that matches the observation. Note that the ability to determine the plasma conditions from these CR calculations requires the most accurate available knowledge of atomic rates and cross sections, accurate treatment of the plasma effects on the ionization distribution and line shapes, and an accurate treatment of the radiation transport. Known discrepancies between measured and calculated line shapes[54] indicate that more benchmark experiments are needed, particularly in the HED regime.

Following this forward calculation search process, Rochau *et al.* determined the time-dependent electron temperature and density of the shocked CH_2 plasma from the Si emission spectra (Fig. 11). The calculations were done using two different CR models: one developed at the Weizmann Institute[52] and one from the SPECT3D software package.[53] As the shock propagates, the electron temperature is shown to decrease from about 400 to 300 eV while the density increases from about 15 to 40 mg/cm^3. These data provide a basis for improving the understanding of the evolution of

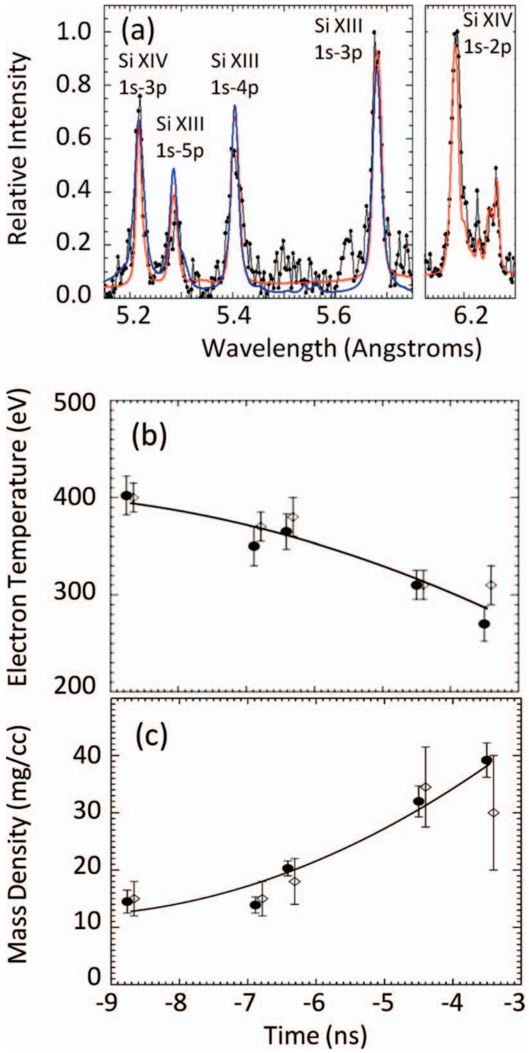

FIG. 11. (Color) (a) The measured Si emission spectrum (black points) from the radiating shock in the ZPDH at $t=-6.8$ ns in comparison to CR models from the Weizmann Institute (red line) and SPECT3D (blue line). (b) Time-dependent electron temperature and (c) mass density of the shocked Si-doped CH_2 during the implosion of the ZPDH inferred from comparisons to Si emission spectra using CR models from the Weizmann Institute (open diamonds) and SPECT3D (solid circles).

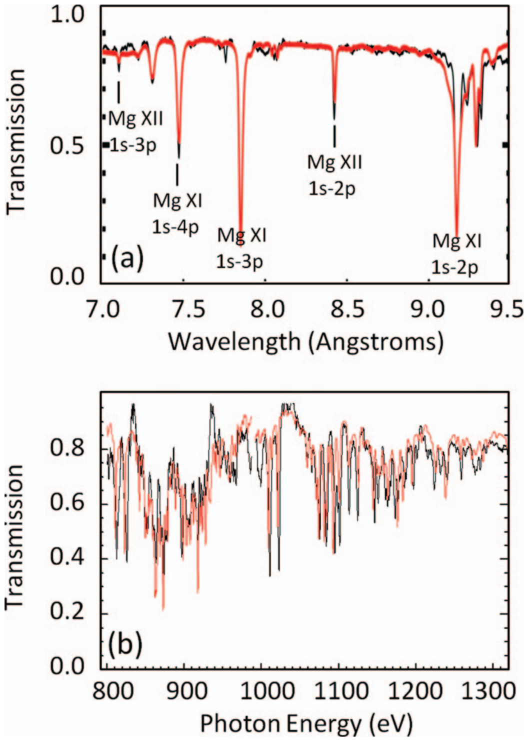

FIG. 12. (Color) (a) Measured Mg K-shell absorption spectrum (black) in comparison to an Opal LTE calculation (red) at $T_e=156$ eV and $n_e=7\times 10^{21}$ cm^{-3}. The Mg is mixed with Fe in a study of the Fe opacity on the ZPDH. (b) Measured Fe L-shell absorption spectrum (black) on the ZPDH in comparison to an Opal LTE calculation (red) at the conditions determined from the Mg comparison in (a).

complex integrated radiation-hydrodynamic plasmas, such as radiating shocks.

VI. HED MEASUREMENTS: FREQUENCY DEPENDENT OPACITY

The opacity of a material, κ, is a determination of its transparency to electromagnetic radiation, which is described by the equation

$$T(h\nu) = \exp[-\kappa(h\nu)\rho x], \quad (5)$$

where T is the transmission through a plasma with density, ρ, and thickness, x. The opacity is a function of photon energy, $h\nu$, due to the structure of the bound electron energy states. It is also a function of temperature and density since the bound energy state structure depends on the ionization state. Opacity is a fundamental material property of importance to all plasmas. For a plasma with a given temperature and density it is important to know the charge state distribution, which transitions are important in determining the opacity and the importance of plasma effects, such as line broadening.

In the ZPDH, x rays emitted by the radiating shock during the implosion can heat a thin sample placed across the upper aperture to temperatures >150 eV [Fig. 9(d)]. When this shock stagnates on the axis it forms a localized, broadband, smooth x-ray source called a backlighter with an equivalent brightness temperature >300 eV. The opacity is experimentally determined through the following process:[55] (1) Measure the backlighter spectrum on an experiment without the sample. (2) Measure the absorption of the backlighter x rays through the sample on a subsequent experiment. (3) Compute the ratio between these two measurements to determine the transmission spectrum assuming reproducibility in the backlighter spectrum. (4) Combine the known areal density with the transmission measurement in Eq. (5) to determine the opacity. Using this platform, Bailey *et al.*[43] measured the transmission of L-shell iron in the photon energy range of 800 eV–1300 eV (Fig. 12). The plasma conditions were determined by mixing in a small amount of magnesium, which was stripped to the K-shell containing mostly H- and He-like ionization states: a realm of atomic physics that is relatively well understood. Comparing the Mg absorption to calculations, Bailey *et al.* were able to determine the temperature and density of the plasma. This Mg/Fe plasma is in local thermodynamic equilibrium (LTE), which is much easier to simulate than the CR calculations presented previously. In the LTE approximation, the ionization states and

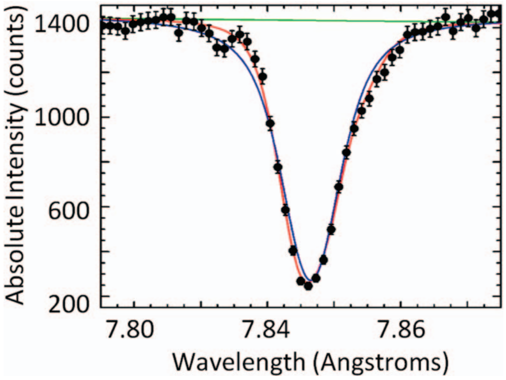

FIG. 13. (Color) Comparison of the measured Mg XI 1s-3p line profile (points) to a best-fit Voigt (blue) and a detailed calculation of the asymmetric Stark profile (red). The reduced chi squared of the Voigt fit is 5.5 and that of the detailed calculation is 1.2. Adapted from Ref. 55.

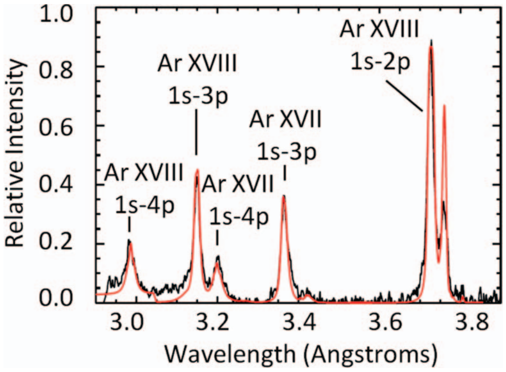

FIG. 14. (Color) Space-integrated Ar emission spectrum measured from an ICF capsule implosion in the ZPDH (black) in comparison to a CR model (red) assuming a uniform sphere with $T_e=940$ eV and $n_e=3\times10^{23}$ cm^{-3}.

populations are determined by the Saha–Boltzmann equations, which depend on both the electron temperature and the electron density. The electron density can be determined separately from analysis of the line shapes through the Stark broadening,[4,5] which then allows the unique determination of the electron temperature using the LTE approximation. It is common to approximate Stark broadened line shapes with Voigt profiles that have a calibrated full width at half maximum. Detailed calculations of the Stark broadening, however, often show asymmetric line profiles.[5] As an example, Fig. 13 shows a comparison between the measured Mg XI 1s-3p line profile to both a best-fit Voigt profile and a detailed calculation of the Stark broadened line shape.[55] Both show good qualitative agreement, but they have significant statistical differences. The Voigt fit and detailed calculation have reduced chi squared of 5.5 and 1.2, respectively, highlighting the quality of the data and the calculation.

In a comparison between the measured Mg transmission and an Opal LTE calculation[56] [Fig. 12(a)], the conditions of the plasma were determined to be $T_e=156$ eV and $n_e=7\times10^{21}$ cm^{-3}. The resulting Fe transmission spectrum at these plasma conditions was compared to many modern LTE opacity calculations and found to be in good agreement.[43] An example comparison between the data and an Opal calculation is shown in Fig. 12(b). The level of agreement indicates that best-effort calculations at these plasma conditions and for this element contain much of the correct physics. Rigorously testing the models requires measurements of different materials and at different conditions, particularly at higher density to test the line broadening models.

VII. HED MEASUREMENTS: INERTIAL CONFINEMENT FUSION

The ZPDH is also a useful platform for studying indirect drive ICF.[44,51,57–59] In this application, an ~2 mm diameter capsule containing ~20 atm of D_2 gas is placed at the center of the CH_2 foam [Fig. 9(e)]. The radiating shock propagating in the CH_2 reaches peak power emission >40 TW and the resulting x-ray preheat makes the entire CH_2 optically thin to its own radiation. The tungsten plasma that surrounds the shock is optically thick, traps the emitted x rays from the radiating shock, and re-emits a large fraction of the x-ray energy back into the cylindrical cavity creating a *Hohlraum*. As the system implodes, the shock emission intensity increases and the *Hohlraum* radius decreases causing the radiation temperature in the cavity (and incident on the ICF capsule) to eventually exceed 200 eV. X rays from both the radiating shock and the re-emission from the tungsten *Hohlraum* wall are absorbed in the ICF capsule shell creating an ablation pressure that compresses the D_2 gas to conditions where fusion occurs. This platform produces record indirect-drive DD neutron yields of $>3\times10^{11}$.

Measuring the conditions of the compressed capsule core is important in understanding the dynamics of the ICF implosion. This is done by doping the D_2 gas with a small amount of Argon and observing the Ar K-shell emission using a time- and one-dimensionally space-resolved spectrometer. In some instances, these measurements are made from multiple orthogonal views in order to measure the symmetry of the compressed core. The most basic analysis of the Ar emission is to space integrate the spectra and determine the emissivity averaged capsule plasma conditions. This is done through comparisons to CR calculations following the forward search algorithm described above under an assumption that the capsule core is a uniform sphere. Figure 14 shows a space-integrated spectrum from a typical ICF capsule implosion on Z compared to a uniform sphere CR calculation indicating emissivity averaged fuel conditions of $T_e=940$ eV and $n_e=3\times10^{23}$ cm^{-3}. This type of analysis was pioneered on laser-imploded capsules starting in the 1970s and steadily employed throughout the past 30 years.[60–64]

The unique aspect of the spectral data from ICF implosions in the ZPDH platform is that they are one-dimensionally space resolved. This provides a measure of the emissivity averaged spectra from multiple slices passing through different locations of the hot capsule core (Fig. 15). The relative change in the spectra can be used to determine the gradients in the capsule fuel conditions. Determining the plasma gradients requires a similar forward calculation search as described above. In this case, the assumed plasma conditions must result in synthetic spectra that simultaneously agree with the multiple space-resolved spectra measured in the experiment. This provides a challenge associated

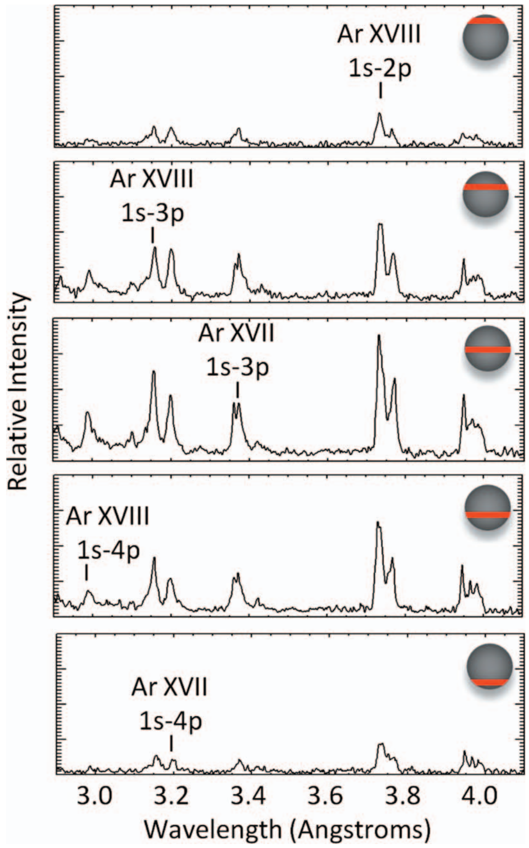

FIG. 15. (Color) Measured spectra averaged over an ~300 ps time period from multiple slices passing through a compressed ICF capsule imploded in the ZPDH. The red band on the sphere in each plot indicates the approximate area of integration relative to the total size of the compressed core.

with the number of calculations required to find a suitable solution. If the plasma conditions are approximated by a one-dimensional sphere containing four radial points, each with a defined T_e and n_e, and each T_e and n_e condition is chosen from 20 possible values, the resulting 2.56×10^{10} possible combinations of plasma conditions make an exhaustive search impractical. Advanced search algorithms such as Pareto genetic algorithms have been successfully employed to determine ICF capsule core conditions on direct-drive laser-imploded capsules using a series of monochromatic images in combination with space-integrated, time-resolved spectra.[65–67] Extending these techniques to the ICF data from the ZPDH platform that is time, space, and fully spectrally resolved may provide better constraints on the plasma density profile from the spatially dependent line shapes.

Another important aspect of space-resolved spectral measurements is that they can provide a signature of spatially dependent mixing between the ICF capsule shell and the fusion fuel. The spatially dependent line shapes provide information on the electron density distribution, the spatially dependent line ratios from neighboring ionization states provide information on the electron temperature, and the spatially dependent intensity of the line emission provides information on the number of Ar ions along each LOS. In a predominantly deuterium plasma, the ratio of electrons to ions is unity. If this ratio is greater than one, then material from the capsule shell, which has a higher atomic number and therefore a higher ratio of electrons to ions, must be mixing in with the capsule fuel. Including the mix fraction in the CR calculations can provide a simultaneous determination of the electron temperature, the mass density, and the fuel fraction. This is work in progress and is left for future publication.

VIII. SUMMARY

Applied spectroscopy provides a powerful diagnostic tool to understand complex pulsed power plasmas including measurements of magnetic fields, electric fields, and the temperature and density conditions of HED plasmas. These measurements probe the fundamental physics of the systems in which they are applied providing a broader scope of information applicable to other areas of physics such as laser produced plasmas and astrophysics. Challenging new applications of spectroscopy to HED plasmas are under development including the extension of magnetic field measurements to high density, nonuniform, and turbulent plasmas and techniques to determine the time-dependent spatial distribution of conditions in complex plasmas. The accurate determination of plasma conditions from recorded spectra depends on the accuracy of atomic theory, the theory of atoms in plasma, and the coupling of these theories with radiation transport. This requires more experiments to benchmark the calculations in the HED regime.

ACKNOWLEDGMENTS

Special thanks to Ray Leeper and Mark Herrmann for their support in the preparation of this manuscript. Sandia is a multiprogram laboratory operated by Sandia Corporation, a Lockheed Martin Co., for the United States Department of Energy under Contract No. DE-AC04-94AL85000.

[1] National Research Council, *Frontiers in High Energy Density Physics: The X-Games Of Contemporary Science* (The National Academies, Washington, D.C., 2003).
[2] S. T. Pai and Q. Zhang, *Introduction to High Power Pulse Technology* (World Scientific, Singapore, 1995).
[3] G. Mesyats, *Pulsed Power* (Springer, New York, 2004).
[4] H. Griem, *Plasma Spectroscopy* (McGraw-Hill, New York, 1964).
[5] H. Griem, *Spectral Line Broadening by Plasmas* (Academic, New York, 1974).
[6] Y. Maron, E. Sarid, E. Nahshoni, and O. Zahavi, Phys. Rev. A **39**, 5856 (1989).
[7] Y. Maron, E. Sarid, O. Zahavi, L. Perelmutter, and M. Sarfarty, Phys. Rev. A **39**, 5842 (1989).
[8] C. Litwin, Y. Maron, and E. Sarid, Phys. Plasmas **1**, 758 (1994).
[9] H. Bluhm and P. Hoppe, Nucl. Instrum. Methods Phys. Res. A **464**, 6 (2001).
[10] R. Arad, K. Tsigutkin, Y. Maron, A. Fruchtman, and J. D. Huba, Phys. Plasmas **10**, 112 (2003).
[11] R. Arad, K. Tsigutkin, Yu. V. Ralchenko, and Y. Maron, Phys. Plasmas **7**, 3797 (2000).
[12] B. Rubinstein, J. Citrin, R. Doron, R. Arad, Y. Maron, and A. Filler, *Proceedings of the 35th EPS Conference on Plasma Physics*, Hersonissos, 9–13 June 2008 (ECA, Lausanne, 2008), Vol. 32D, p. O4.055.
[13] A. S. Kingsep, K. V. Chukbar, and V. V. Yan'kov, Rev. Plasma Phys. **16**, 243 (1990).
[14] A. Fruchtman, Phys. Fluids B **3**, 1908 (1991).
[15] B. V. Weber, J. R. Boller, and R. J. Commisso, J. Appl. Phys. **45**, 1043 (1984).
[16] M. Sarfaty, Y. Maron, Ya. E. Krasik, A. Weingarten, R. Arad, R. Shpitalnik, and A. Fruchtman, Phys. Plasmas **2**, 2122 (1995).

[17] R. Shpitalnik, A. Weingarten, K. Gomberoff, Ya. Krasik, and Y. Maron, Phys. Plasmas **5**, 792 (1998).
[18] G. Davara, L. Gregorian, E. Kroupp, and Y. Maron, Phys. Plasmas **5**, 1068 (1998).
[19] L. Gregorian, V. A. Bernshtam, E. Kroupp, G. Davara, and Y. Maron, Phys. Rev. E **67**, 016404 (2003).
[20] L. Gregorian, E. Kroupp, G. Davara, A. Starobinets, V. I. Fisher, V. A. Bernshtam, Yu. V. Ralchenko, Y. Maron, A. Fisher, and D. H. H. Hoffmann, Phys. Rev. E **71**, 056402 (2005).
[21] L. Gregorian, G. Davara, E. Kroupp, A. Starobinets, V. Bernshtam, Yu. V. Ralchenko, and Y. Maron, Phys. Plasmas **12**, 092704 (2005).
[22] E. Stambulchik, K. Tsigutkin, and Y. Maron, Phys. Rev. Lett. **98**, 225001 (2007).
[23] Y. Maron, M. D. Coleman, D. A. Hammer, and H. S. Peng, Phys. Rev. Lett. **57**, 699 (1986).
[24] Y. Maron, M. D. Coleman, D. A. Hammer, and H. S. Peng, Phys. Rev. A **36**, 2818 (1987).
[25] T. M. Antonsen and E. Ott, Phys. Fluids **19**, 52 (1976).
[26] M. Desjarlais, Phys. Rev. Lett. **59**, 2295 (1987).
[27] J. E. Bailey, A. B. Filuk, A. L. Carlson, D. J. Johnson, P. Lake, E. J. McGuire, T. A. Mehlhorn, T. D. Pointon, T. J. Renk, W. A. Stygar, and Y. Maron, Phys. Rev. Lett. **74**, 1771 (1995).
[28] J. P. Vandevender and D. L. Cook, Science **232**, 831 (1986).
[29] Y. Maron, M. D. Coleman, D. A. Hammer, and H. S. Peng, J. Appl. Phys. **61**, 4781 (1987).
[30] A. B. Filuk, J. E. Bailey, A. L. Carlson, D. J. Johnson, P. Lake, T. A. Mehlhorn, L. P. Mix, T. J. Renk, W. A. Styger, and Y. Maron, Phys. Rev. Lett. **77**, 3557 (1996).
[31] A. Filuk and J. E. Bailey, private communication (2009).
[32] J. E. Bailey, A. B. Filuk, A. L. Carlson, D. J. Johnson, P. Lake, E. J. McGuire, T. A. Mehlhorn, T. D. Pointon, T. J. Renk, W. A. Stygar, Y. Maron, and E. Stambulchik, AIP Conf. Proc. **381**, 245 (1996).
[33] D. Fisher, Y. Maron, and L. P. Petaevskii, Phys. Rev. A **58**, 2214 (1998).
[34] E. Stambulchik, Y. Maron, J. E. Bailey, and M. E. Cuneo, Phys. Rev. A **65**, 052726 (2002).
[35] C. Deeney, T. J. Nash, R. B. Spielman, J. F. Seamen, G. A. Chandler, K. W. Struve, J. L. Porter, W. A. Stygar, J. S. McGurn, D. O. Jobe, T. L. Gilliland, J. A. Torres, M. F. Vargas, L. E. Ruggles, S. Breeze, R. C. Mock, M. R. Douglas, D. L. Fehl, D. H. McDaniel, M. K. Matzen, D. L. Peterson, W. Matsuka, N. F. Roderick, and J. J. MacFarlane, Phys. Rev. E **56**, 5945 (1997).
[36] T. W. L. Sanford, G. O. Allshouse, B. M. Marder, T. J. Nash, R. C. Mock, R. B. Spielman, J. F. Seamen, J. S. McGurn, D. Jobe, T. L. Gilliland, M. Vargas, K. W. Struve, W. A. Stygar, M. R. Douglas, M. K. Matzen, J. H. Hammer, J. S. De Groot, J. L. Eddleman, D. L. Peterson, D. Mosher, K. G. Whitney, J. W. Thornhill, P. E. Pulsifer, J. P. Apruzese, and Y. Maron, Phys. Rev. Lett. **77**, 5063 (1996).
[37] R. B. Spielman, C. Deeney, G. A. Chandler, M. R. Douglas, D. L. Fehl, M. K. Matzen, D. H. McDaniel, T. J. Nash, J. L. Porter, T. W. L. Sanford, J. F. Seamen, W. A. Stygar, K. W. Struve, S. P. Breeze, J. S. McGurn, J. A. Torres, D. M. Zagar, T. L. Gilliland, D. O. Jobe, J. L. McKenney, R. C. Mock, M. Vargas, T. Wagoner, and D. L. Peterson, Phys. Plasmas **5**, 2105 (1998).
[38] C. Deeney, M. R. Douglas, R. B. Spielman, T. J. Nash, D. L. Peterson, P. L. Eplatteneir, G. A. Chandler, J. F. Seamen, and K. W. Struve, Phys. Rev. Lett. **81**, 4883 (1998).
[39] M. D. Knudson, M. P. Desjarlais, and D. H. Dolan, Science **322**, 1822 (2008).
[40] M. D. Knudson, D. L. Hanson, J. E. Bailey, C. A. Hall, J. R. Asay, and W. W. Anderson, Phys. Rev. Lett. **87**, 225501 (2001).
[41] M. E. Foord, R. F. Heeter, P. A. M. van Hoof, R. S. Thoe, J. E. Bailey, M. E. Cuneo, H.-K. Chung, D. A. Liedahl, K. B. Fournier, G. A. Chandler, V. Jonauskas, R. Kisielius, L. P. Mix, C. Ramsbottom, P. T. Springer, F. P. Keenan, S. J. Rose, and W. H. Goldstein, Phys. Rev. Lett. **93**, 055002 (2004).
[42] G. A. Rochau, J. E. Bailey, Y. Maron, G. A. Chandler, G. S. Dunham, D. V. Fisher, V. I. Fisher, R. W. Lemke, J. J. MacFarlane, K. J. Peterson, D. G. Schroen, S. A. Slutz, and E. Stambulchik, Phys. Rev. Lett. **100**, 125004 (2008).
[43] J. E. Bailey, G. A. Rochau, C. A. Iglesias, J. Abdallah, J. J. MacFarlane, I. Golovkin, P. Wang, R. C. Mancini, P. W. Lake, T. C. Moore, M. Bump, O. Garcia, and S. Mazevet, Phys. Rev. Lett. **99**, 265002 (2007).
[44] J. E. Bailey, G. A. Chandler, S. A. Slutz, G. R. Bennett, G. Cooper, J. S. Lash, S. Lazier, R. Lemke, T. J. Nash, D. S. Nielsen, T. C. Moore, C. L. Ruiz, D. G. Schroen, R. Smelser, J. Torres, and R. A. Vesey, Phys. Rev. Lett. **89**, 095004 (2002).
[45] D. L. Peterson, R. L. Bowers, W. Matuska, K. D. McLenithan, G. A. Chandler, C. Deeney, M. S. Derzon, M. Douglas, M. K. Matzen, T. J. Nash, R. B. Spielman, K. W. Struve, W. A. Stygar, and N. F. Roderick, Phys. Plasmas **6**, 2178 (1999).
[46] T. W. L. Sanford, R. E. Olson, R. L. Bowers, G. A. Chandler, M. S. Derzon, D. E. Hebron, R. J. Leeper, R. C. Mock, T. J. Nash, D. L. Peterson, L. E. Ruggles, W. W. Simpson, K. W. Struve, and R. A. Vesey, Phys. Rev. Lett. **83**, 5511 (1999).
[47] R. W. Lemke, J. E. Bailey, G. A. Chandler, T. J. Nash, S. A. Slutz, and T. A. Mehlhorn, Phys. Plasmas **12**, 012703 (2005).
[48] J. E. Bailey, G. A. Chandler, R. C. Mancini, S. A. Slutz, G. A. Rochau, M. Bump, T. J. Buris-Mog, G. Cooper, G. Dunham, I. Golovkin, J. D. Kilkenny, P. W. Lake, R. J. Leeper, R. Lemke, J. J. MacFarlane, T. A. Mehlhorn, T. C. Moore, T. J. Nash, A. Nikroo, D. S. Nielsen, K. L. Peterson, C. L. Ruiz, D. G. Schroen, D. Steinman, and W. Varnum, Phys. Plasmas **13**, 056301 (2006).
[49] R. R. Peterson, D. L. Peterson, R. G. Watt, G. Idzorek, T. Tierney, and M. Lopez, Phys. Plasmas **13**, 056901 (2006).
[50] J. E. Bailey, G. A. Rochau, R. C. Mancini, C. A. Iglesias, J. J. MacFarlane, I. E. Golovkin, C. Blancard, Ph. Cosse, and G. Faussurier, Phys. Plasmas **16**, 058101 (2009).
[51] G. A. Rochau, J. E. Bailey, G. A. Chandler, G. Cooper, G. S. Dunham, P. W. Lake, R. J. Leeper, R. W. Lemke, T. A. Mehlhorn, A. Nikroo, K. J. Peterson, C. L. Ruiz, D. G. Schroen, S. A. Slutz, D. Steinman, W. A. Stygar, and W. Varnum, Plasma Phys. Controlled Fusion **49**, B591 (2007).
[52] V. I. Fisher, D. V. Fisher, and Y. Maron, High Energy Density Phys. **3**, 283 (2007).
[53] J. J. MacFarlane, I. E. Golovkin, P. Wang, P. R. Woodruff, and N. A. Pereyra, High Energy Density Phys. **3**, 181 (2007).
[54] S. Glenzer and H. J. Kunze, Phys. Rev. A **53**, 2225 (1996).
[55] J. E. Bailey, G. A. Rochau, R. C. Mancini, C. A. Iglesias, J. J. MacFarlane, I. E. Golovkin, J. C. Pain, F. Gilleron, C. Blancard, Ph. Cosse, G. Faussurier, G. A. Chandler, T. J. Nash, D. S. Nielsen, and P. W. Lake, Rev. Sci. Instrum. **79**, 113104 (2008).
[56] C. A. Iglesias and F. J. Rogers, Astrophys. J. **464**, 943 (1996).
[57] J. E. Bailey, G. A. Chandler, S. A. Slutz, I. Golovkin, P. W. Lake, J. J. MacFarlane, R. C. Mancini, T. J. Burris-Mog, G. Cooper, R. J. Leeper, T. A. Mehlhorn, T. C. Moore, T. J. Nash, D. S. Nielsen, C. L. Ruiz, D. G. Schroen, and W. A. Varnum, Phys. Rev. Lett. **92**, 085002 (2004).
[58] C. L. Ruiz, G. W. Cooper, S. A. Slutz, J. E. Bailey, G. A. Chandler, T. J. Nash, T. A. Mehlhorn, R. J. Leeper, D. Fehl, A. J. Nelson, J. Franklin, and L. Ziegler, Phys. Rev. Lett. **93**, 015001 (2004).
[59] S. A. Slutz, K. J. Peterson, R. A. Vesey, R. W. Lemke, J. E. Bailey, W. Varnum, C. L. Ruiz, G. W. Cooper, G. A. Chandler, G. A. Rochau, and T. A. Mehlhorn, Phys. Plasmas **13**, 102701 (2006).
[60] B. Yaakobi, D. Steel, E. Thorsos, A. Hauer, and B. Perry, Phys. Rev. Lett. **39**, 1526 (1977).
[61] J. D. Kilkenny, R. W. Lee, M. H. Key, and J. G. Lunney, Phys. Rev. A **22**, 2746 (1980).
[62] B. A. Hammel, C. J. Keane, M. D. Cable, D. R. Kania, J. D. Kilkenny, R. W. Lee, and R. Pasha, Phys. Rev. Lett. **70**, 1263 (1993).
[63] C. J. Keane, B. A. Hammel, A. L. Osterheld, and D. R. Kania, Phys. Rev. Lett. **72**, 3029 (1994).
[64] S. P. Regan, J. A. Delettrez, F. J. Marshall, J. M. Soures, V. A. Smalyuk, B. Yaakobi, R. Epstein, V. Yu. Glebov, P. A. Jaanimagi, D. D. Meyerhofer, P. B. Radha, T. C. Sangster, W. Seka, S. Skupsky, C. Stoeckl, R. P. J. Town, D. A. Haynes, I. E. Golovkin, C. F. Hooper, J. A. Frenje, C. K. Li, R. D. Petrasso, and F. H. Seguin, Phys. Rev. Lett. **89**, 085003 (2002).
[65] I. Golovkin, R. Mancini, S. Louis, Y. Ochi, K. Fujita, H. Nishimura, H. Shirga, N. Miyanaga, H. Azechi, R. Butzbach, I. Uschmann, E. Forster, J. Delettrez, J. Koch, R. W. Lee, and L. Klein, Phys. Rev. Lett. **88**, 045002 (2002).
[66] L. Welser-Sherrill, R. C. Mancini, J. A. Koch, N. Izumi, R. Tommasini, S. W. Haan, D. A. Haynes, I. E. Golovkin, J. J. MacFarlane, J. A. Delettrez, F. J. Marshall, S. P. Regan, V. A. Smalyuk, and G. Kyrala, Phys. Rev. E **76**, 056403 (2007).
[67] J. A. Koch, N. Izumi, L. A. Welser, R. C. Mancini, S. W. Haan, R. W. Lee, P. A. Amendt, T. W. Barbee, S. Dalhed, K. Fujita, I. E. Golovkin, L. Klein, O. L. Landen, F. J. Marshall, D. D. Meyerhofer, H. Nishimura, Y. Ochi, S. Regan, T. C. Sangster, V. Smalyuk, and R. Tommasini, High Energy Density Phys. **4**, 1 (2008).